Surfaces and Interfaces 95 (2026) 109836

Contents lists available at ScienceDirect

Surfaces and Interfaces

journal homepage: www.sciencedirect.com/journal/surfaces-and-interfaces

Interfacial passivation of non-fullerene electron transporting thin films via polymer surface engineering for perovskite solar cells

Shih-Han Huang [a], Wen-Ting Li [b], Chia-Feng Li [b,c], Yu-Hung Hsiao [b,c], Hou-Chin Cha [a,d], Chih-Min Chuang [e], Yu-Ching Huang [a,b,f,*]

[a] Organic Electronics Research Center, Ming Chi University of Technology, New Taipei City 24301, Taiwan
[b] Department of Materials Engineering, Ming Chi University of Technology, New Taipei City 24301, Taiwan
[c] Department of Materials Science and Engineering, National Taiwan University, Taipei 10617, Taiwan
[d] College of Engineering, Ming Chi University of Technology, New Taipei City 24301, Taiwan
[e] Department of Physics, National Atomic Research Institute, Taoyuan City 325207, Taiwan
[f] Center for Sustainability and Energy Technologies, Chang Gung University, Taoyuan City 33302, Taiwan

ARTICLE INFO

Keywords:
Inverted structure
Perovskite solar cells
Interfacial modification
Non-fullerene acceptor
Surface passivation

ABSTRACT

Inverted perovskite solar cells (PSCs) traditionally rely on fullerene-based materials as electron transport layers (ETLs). However, emerging non-fullerene acceptors (NFAs), such as the end-fluorinated ITIC-4F, offer superior mechanical robustness and potential for scalable coating. In this work, we investigate the interfacial properties and film quality of ITIC-4F as a fullerene-free ETL. Despite suitable energy alignment, drive-level capacitance profiling (DLCP) and light-intensity analysis indicate that pristine ITIC-4F coatings exhibit high trap densities, causing severe recombination and limiting the average efficiency to 3.24%. To overcome these surface limitations, we employed a thin poly(methyl methacrylate) (PMMA) passivation layer to engineer the perovskite/ETL interface. Systematic optimization of the PMMA coating effectively suppressed surface trap states and improved the physical contact quality. Consequently, this interfacial engineering strategy significantly boosted the average power conversion efficiency (PCE) to 11.47%, with a champion PCE of 13.87%. Comprehensive transient optoelectronic analysis confirmed that the PMMA-modified interface exhibits reduced electronic defect states and enhanced carrier lifetimes. These results demonstrate that strategic surface engineering with insulating polymers is essential for unlocking the potential of NFA-based coatings in efficient, fullerene-free photovoltaics.

1. Introduction

Perovskite solar cells (PSCs) have achieved remarkable power conversion efficiencies (PCE) exceeding 27%, showing their significant potential for industrial commercialization [1–4]. The inverted (p-i-n) architecture has emerged as a preferred configuration due to its widespread adoption and compatibility with various perovskite-based tandem device structures [5,6]. In these inverted devices, electron transporting layers (ETLs) typically utilize fullerenes deposited via vacuum evaporation and [6,6]-phenyl-C61-butyric acid methyl ester (PCBM) processed through solution coating [7–11]. However, compared to the diverse range of available hole transporting layers (HTLs), ETL materials remain relatively limited, despite their critical role in dominating overall device performance. Although fullerene derivatives have been the standard, they face critical challenges regarding coating quality and stability. Their spherical structure often leads to restricted solubility and poor film uniformity over large areas [12–14]. Furthermore, mechanical fragility and susceptibility to halogen diffusion across the interface compromise the long-term integrity of the ETL coating, driving the urgent need for alternative materials that offer both superior electronic properties and robust film-forming capabilities [15,16].

The development of diverse non-fullerene acceptors (NFAs) has broadened the material candidates for high-performance organic solar cells [17,18]. NFAs provide enhanced electron mobility and hydrophobicity, which are beneficial for improving surface wettability and suppressing moisture-induced degradation. Specifically, perylene diimides (PDI), naphthalene imide (NDI) derivatives leverage rigid π-skeletons for high electron affinity and efficient carrier transport, employing side-chain engineering to optimize solubility and energy level matching [19,20]. Compared to traditional fullerenes, NFAs exhibit superior

* Corresponding author at: Organic Electronics Research Center, Ming Chi University of Technology, New Taipei City 24301, Taiwan.
E-mail address: huangyc@mail.mcut.edu.tw (Y.-C. Huang).

https://doi.org/10.1016/j.surfin.2026.109836
Received 18 January 2026; Received in revised form 22 April 2026; Accepted 10 June 2026
Available online 11 June 2026

molecular stacking and morphological stability, demonstrating minimal surface roughness changes even under thermal stress. However, a critical bottleneck remains in their solution processing; large planar conjugated frameworks are prone to excessive aggregation, leading to pinholes and non-uniform interfacial contact. Such discontinuous film coverage results in high defect densities that compromise the device performance [21]. While strategies like 3D twisted architectures or dipole engineering (e.g., in Y6 derivatives) have been employed to optimize molecular assembly and film morphology [22–24]. This strategy facilitates ordered molecular assembly through supramolecular interactions and enhances hot-electron extraction. Consequently, these NFAs achieved a remarkable PCE of 25.59%, demonstrating their superior potential compared to traditional fullerene-based ETLs [25].

From an economic perspective, the ITIC remains highly attractive due to superior solution processability and lower material cost compared to Y6 derivatives. However, ITIC-based ETLs suffer from poor hole-blocking capability. This limitation is attributed to the relatively shallow highest occupied molecular orbital (HOMO) level of ITIC, which lacks a sufficient energetic offset from the perovskite absorber [26,27]. To overcome this electronic limitation while retaining processability, end-fluorinated ITIC-4F has emerged as a promising candidate. The introduction of fluorine atoms deepens the HOMO level, theoretically enhancing hole-blocking efficiency. Nevertheless, realizing high-quality ITIC-4F coatings presents a new set of interfacial challenges. Unlike blended systems or vacuum-deposited films, pristine ITIC-4F coatings on perovskite often exhibit high surface trap densities and imperfect physical contact, which hinder carrier extraction [28,29]. Addressing these interfacial deficiencies is crucial for mitigating recombination losses and facilitating charge transport within NFA-based architectures.

In this work, we investigate the interfacial properties and film quality of ITIC-4F as a fullerene-free ETL. Although ITIC-4F exhibits favorable energetics, our evaluations, including drive-level capacitance profiling (DLCP) and light-intensity analysis, reveal that pristine ITIC-4F coatings are plagued by severe interfacial defects and high trap densities. To repair these surface imperfections, we employed a thin poly(methyl methacrylate) (PMMA) passivation layer to engineer the perovskite/ETL interface. Systematic optimization of the PMMA coating effectively suppressed surface trap states and reconstructed the physical contact, boosting the average PCE from 3.24% to 11.47%, with a champion PCE of 13.87%. Comprehensive transient optoelectronic analysis confirmed that this strategic surface engineering reduced electronic defect states and improved carrier lifetimes. This study demonstrates that utilizing insulating polymers for interfacial passivation is a robust pathway to enable high-quality, fullerene-free NFA coatings for efficient PSCs.

2. Experimental section

2.1. Materials

The end-fluorinated NFA as ITIC-4F (99%) was purchased from 1-Materials. Perovskite precursors, including formamidinium iodide (FAI, 99.99%), formamidinium bromide (FABr, 99.99%), methylammonium iodide (MAI, 99.99%), methylammonium chloride (MACl, 99.99%), and 2-thiopheneethylamine hydrochloride (TEACl, 99.99%), were obtained from Greatcell Solar Materials. Lead iodide (PbI_2, 99.999%) and the self-assembled monolayer molecule MeO-2PACz (>98%) were sourced from TCI Chemical. PMMA (average M_w 350,000), bathocuproine (BCP, 96%), and anhydrous solvents, including chlorobenzene (CB, 99.9%), isopropanol (IPA, 99.5%), dimethylformamide (DMF, ≥99.9%), and ethanol (EtOH, 99.8%), were purchased from Sigma-Aldrich. PCBM was purchased from Lumtec. All chemicals were used as received without further purification.

2.2. Device fabrication

Inverted p-i-n structured solar cells were fabricated on pre-cleaned fluorine-doped tin oxide (FTO) coated glass substrates, which were sequentially cleaned via ultrasonic treatment. For the HTL, a MeO-2PACz solution (1 mM in anhydrous EtOH) was spin-coated onto the FTO at 3000 rpm for 20 s and subsequently annealed at 100 °C for 5 min. The perovskite active layer was deposited using the anti-solvent quenching method, and with the precursor formulation and processing parameters adapted from previously reported procedures [30]. A 1.4 M perovskite precursor solution (50 μl) was spin-coated onto the SAM-modified substrates using a two-step program: 1000 rpm for 10 s followed by 5000 rpm for 30 s. During the second step, 300 μl of ethyl acetate was rapidly deposited 18 s after the start of the spin cycle. The resulting wet films were immediately transferred to a hotplate and annealed at 150 °C for 10 min. For the interfacial modification, PMMA was dissolved in CB at various concentrations and spin-coated onto the annealed perovskite surface at 5000 rpm for 30 s to form an ultrathin passivation coating. The ETL, either ITIC-4F (10 mg/ml) or PCBM (20 mg/ml) in CB, was then spin-coated over the PMMA-modified surface at 1000 rpm for 30 s. A BCP buffer layer (0.1 wt% in IPA) was deposited at 3000 rpm for 20 s to tune the work function. Finally, a 100 nm Silver (Ag) electrode was thermally evaporated under high vacuum ($<10^{-6}$ Torr) through a shadow mask, defining an active area of 0.09 cm^2.

2.3. Characterization

Photovoltaic performance was evaluated via current density–voltage (J–V) measurements using a solar simulator under AM 1.5 G illumination (100 mW cm^{-2}). Interfacial and bulk electronic properties, including capacitance–voltage (C–V), transient photovoltage (TPV), transient photocurrent (TPC), electrochemical impedance spectroscopy (EIS), and drive-level capacitance profiling (DLCP) were characterized using an all-in-one electrical measurement platform (Paios, Fluxim). The DLCP measurements were conducted with the DC bias scanned from −0.2 V to 1.25 V while varying the AC amplitude from 10 mV to 50 mV at a representative frequency of 50 kHz. The EIS spectra were acquired by superimposing an AC voltage of 50 mV onto a fixed DC bias maintained at the device's V_{OC}. The resulting AC current response was recorded over a frequency range from 1 MHz to 10 Hz to determine the total complex impedance (Z). These techniques were utilized to quantify the defect density and evaluate the charge-carrier dynamics across the multi-layered coating interfaces.

3. Results and discussions

Most p-i-n structure PSCs use fullerene derivative PCBM as ETL. Due to the complex synthesis process, fullerene is not an ideal candidate for commercialization. Recently, NFAs have emerged as promising alternatives owing to their highly controllable electronic properties [31]. Specifically, A-D-A type NFAs featured a fused-ring core with attached side chains and two compact, strong electron-withdrawing end groups. ITIC possesses a comparable LUMO of −3.83 eV, comparable to that of PCBM (−3.95 eV) [32,33]. While ITIC exhibits promising electron-transporting alignment with the perovskite energy levels, its relatively high HOMO level of −5.48 eV is insufficient for effective hole blocking. In contrast, the addition of fluorinated group enhances the electron-withdrawing capability, resulting in a deeper HOMO level. Therefore, ITIC-4F exhibits a HOMO level of −5.66 eV, providing superior hole-blocking ability compared to ITIC [34]. The chemical structure of ITIC-4F is shown in Fig. 1a. To evaluate the film-forming properties and interfacial compatibility of ITIC-4F, the layers were prepared using the concentration of 5, 10, 15, and 20 mg/ml in chlorobenzene (denoted as ITIC-4F-5 to ITIC-4F-20). The J-V curves of the champion devices are shown in Fig. 1b. Statistical distributions of the photovoltaic parameters are presented in Fig. 1c-f and summarized in Table 1. The control PSCs utilizing PCBM achieved an average power conversion efficiency (PCE) of 16.75%±1.29%, with a V_{oc} of 1.14±0.01 V, a short-circuit current density (J_{sc}) of 20.17±0.59 mA cm^{-2}, and a FF

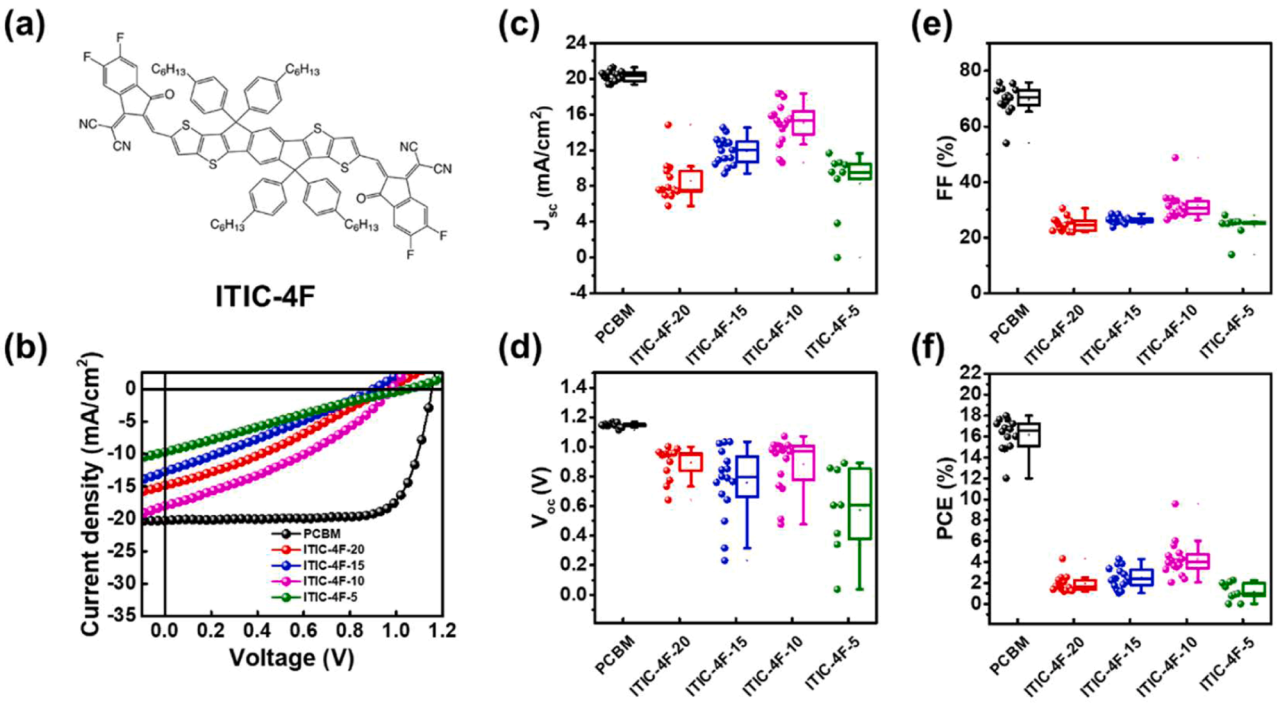

Fig. 1. Optimization of the ITIC-4F electron-transporting layer. (a) Chemical structure of ITIC-4F. (b) J−V curves of the champion devices, (c–f) Statistical distribution of photovoltaic parameters of PSCs utilizing a PCBM control and ITIC-4F layers deposited from different concentrations (5, 10, 15, and 20 mg/ml).

Table 1
Device performance of PSCs fabricated with different ITIC-4F concentrations and PCBM control.

ETL	Concentration (mg/ml)	V_{oc} (V)	J_{sc} (mA/cm^2)	FF (%)	PCE (%)	R_s (ohm)	R_{sh} (ohm)
PCBM	20	1.14±0.01 (1.14)	20.17±0.59 (20.81)	72.78±3.74 (75.86)	16.75±1.29 (18.01)	72.35±15.01 (55.75)	5256.66±2398.17 (12,089.40)
ITIC-4F	20	0.91±0.07 (0.96)	7.63±1.96 (14.86)	23.6 ± 2.38 (30.52)	1.65±0.56 (4.33)	1238,931.62±3714,090.93 (1374.28)	907,439.35±2719,411.26 (1228.35)
	15	0.70±0.25 (1.03)	11.5 ± 1.68 (14.54)	26.28±1.43 (28.6)	2.32±1.05 (4.29)	2158,964.27±7477,055.18 (213.18)	812,154.83±2809,201.58 (2531.17)
	10	0.89±0.12 (1.07)	15.23±1.81 (18.32)	29.71±2.62 (48.78)	4.11±1.13 (9.57)	254.00±129.27 (148.56)	1754.77±955.08 (3538.95)
	5	0.57±0.30 (0.60)	8.32±3.84 (10.37)	24.14±4.09 (25.79)	1.19±0.86 (2.26)	206.45±78.59 (980.3887)	604.34±780.6 (1018.712)

of 72.78±3.75. In contrast, the devices with thickest coating (ITIC-4F-20) exhibited significantly lower performance, with an average PCE of 1.65%±0.56%, V_{oc} of 0.91±0.07 V, J_{sc} of 7.63±1.96, and FF of 23.6%±2.38%. These poor results are attributed to the excessive film thickness, which introduces significant bulk resistance and hinders vertical charge transport across the interface. Reducing the concentration to 15 mg/ml and 10 mg/ml, improved the average PCE improved to 2.32%±1.05% and 4.11%±1.13%, primarily driven by the recovery of J_{sc} to 11.50±1.68 mA cm^{-2} and 15.23±1.81 mA cm^{-2}. However, further reducing the concentration to 5 mg/ml failed to yield additional improvements. This suggests that at such low concentrations, the deposited material is insufficient to form an effective hole-blocking layer across the perovskite surface. The lack of coverage likely creates shunting pathways (direct contact between HTL and ETL), which is consistent with the observed low FF and V_{oc}. Consequently, 10 mg/ml concentration was identified as the optimal concentration to achieve a uniform functional interface for subsequent experiments.

To quantitatively evaluate these charge transport properties, space-charge limited current (SCLC) measurements were performed on electron-only devices (**Figure S1**). The results reveal that electron mobility (μ_e) is highly sensitive to the ITIC-4F concentration. At a low concentration of 5 mg/mL, the resulting film was insufficiently continuous and too thin, leading to significant leakage current fluctuations that hindered reliable SCLC analysis. It is worth noting that the electron mobility improved as the concentration increased from 10 to 20 mg/mL, which is likely attributed to denser molecular stacking. However, this improvement did not lead to a higher device PCE. To provide direct visual evidence of the relationship between ITIC-4F concentration and film quality, atomic force microscopy (AFM) was employed to examine the surface topography and continuity of the resulting films. As illustrated in **Figure S2**, the film morphology varies significantly with solution concentration. At 5 mg/ml, 15 mg/ml, and 20 mg/ml, the films exhibit high root-mean-square (RMS) roughness values of 30.98 nm, 17.32 nm, and 22.62 nm, respectively. These elevated values suggest substantial surface fluctuations or molecular aggregation, potentially hindering efficient interfacial contact. Conversely, the optimized 10 mg/ml concentration yields a smooth, continuous, and pinhole-free morphology with a minimum RMS roughness of 8.97 nm. This marked improvement in uniformity confirms that a 10 mg/ml concentration is essential for achieving a compact functional interface.

To further elucidate the recombination dynamics and interfacial quality of the ITIC-4F coatings, a light-intensity-dependent analysis of the photovoltaic parameters was conducted. This method provides a facile and effective approach for evaluating carrier recombination and

extraction mechanisms under different light illuminations [35,36]. Ideally, V_{oc} exhibits a logarithmic increase with light intensity (ln(I)), while J_{sc} scales linearly, with deviations indicating inefficient exciton dissociation or extraction losses. Deviations from these trends typically indicate inefficient exciton dissociation or extraction losses. The FF, however, exhibits a complex dependence on intensity, representing a balance between extraction velocity and recombination. Notably, a collapse in FF at low light intensities is a signature of dominant shunt resistance, often arising from pinholes or structural imperfections in the functional layers. Fig. 2a-d illustrates the device parameters under light intensities ranging from 100 to 1 mW cm^{-2}. While the V_{oc} and J_{sc} trends for both PCBM and ITIC-4F samples follow standard logarithmic and linear decays without significant variation, the FF behavior reveals distinct differences in film integrity. The PCBM-based PSC shows a rising FF as intensity decreases from 100 mW cm^{-2}, stabilizing at lower intensities. This indicates that the PCBM device is primarily limited by series resistance at high intensity but maintains a robust, leak-free interface at low intensity. In contrast, the FF for ITIC-4F-20 and ITIC-4F-15 devices collapses immediately as intensity reduces, confirming the presence of severe shunting pathways attributed to the poor coating coverage identified in the previous section. For the optimized ITIC-4F-10 device, the FF initially follows the PCBM trend but begins to collapse, dropping from 47.03% to 36.13%, as intensity reduces from 10 to 1 mW cm^{-2}. This degradation suggests that despite optimized concentrations, substantial interfacial losses persist between the perovskite and ITIC-4F layers, necessitating further diagnostic investigation. To monitor the spatial and energetic distribution of trap states, we employed DLCP [37]. Unlike conventional C–V profiling, DLCP isolates the bulk carrier and trap density from interface states by accounting for the non-linear capacitance response to the AC excitation amplitude (δ_V). Fig. 2e displays the trap density profiles for PCBM and ITIC-4F-10 devices (structure: FTO/MeO-2PACz/Perovskite/ETL/BCP/Ag). Both samples exhibit a characteristic U-shaped trap distribution, where the profiling depth correlates to the spatial location within the perovskite layer, moving from the ETL interface toward the HTL interface. The PCBM-based device demonstrates a superior electronic profile, with a minimum bulk trap density of approximately 3×10^{18} cm^{-3} at a depth of 250–300 nm. The primary issue identified in the ITIC-4F is a significant elevation in the trap density compared to the PCBM. Within the film bulk (approx. 300–350 nm), the ITIC-4F-10 device displays a minimum trap density of roughly 9×10^{18} cm^{-3}, which is nearly a threefold increase over the PCBM reference. This indicates that ITIC-4F is less effective at passivating surface defects or grain boundaries during film formation. Furthermore, the profiling depth range for ITIC-4F is notably restricted (280–410 nm), failing to probe the region closer to the ETL interface (150–250 nm) that the PCBM device successfully characterizes. This contraction of the depletion region suggests a higher background carrier concentration or a collapse of the internal electric field near the front contact, which likely impedes efficient charge extraction. At the HTL/perovskite (HTL/PVSK) interface (depth > 400 nm), both devices show a sharp divergence in defect states, but the ITIC-4F curve consistently maintains a higher magnitude. The cumulative evidence suggests that substituting PCBM with ITIC-4F introduces a higher density of deep-level recombination centers throughout the active layer and at the interfaces. These spatially resolved defects provide a clear physical explanation for the anticipated losses in V_{oc} and FF in the ITIC-4F-based devices, highlighting a need for further interfacial engineering or additive optimization.

Addressing the high trap density and interfacial recombination identified in the ITIC-4F devices, we introduced an insulating polymer interlayer to passivate the surface defects. As demonstrated by Seok et al., a thin layer of PMMA can effectively passivate surface trap states on perovskite films, leading to a significant reduction in trap density and enhanced device performance [38]. In this architecture, the PMMA interlayer at the perovskite/ITIC-4F junction serves a dual purpose: isolating the perovskite interface from degradation sources and physically smoothing the surface morphology to ensure uniform ETL deposition. To optimize this interfacial modification, PMMA layers were spin-coated from solutions with concentrations of 0.25, 0.50, 0.75, and 1.00 mg/ml prior to ITIC-4F deposition. The statistic distributions of photovoltaic parameters are showed in Fig. 3 and summarized in Table 2. The reference devices without PMMA (pristine) exhibited a relatively poor average PCE of 3.24%±2.97%, V_{oc} of 0.51±0.33 V, J_{sc} of 16.45±3.68 mA cm^{-2}, and FF of 30.41±6.91%. Upon introducing a 0.25

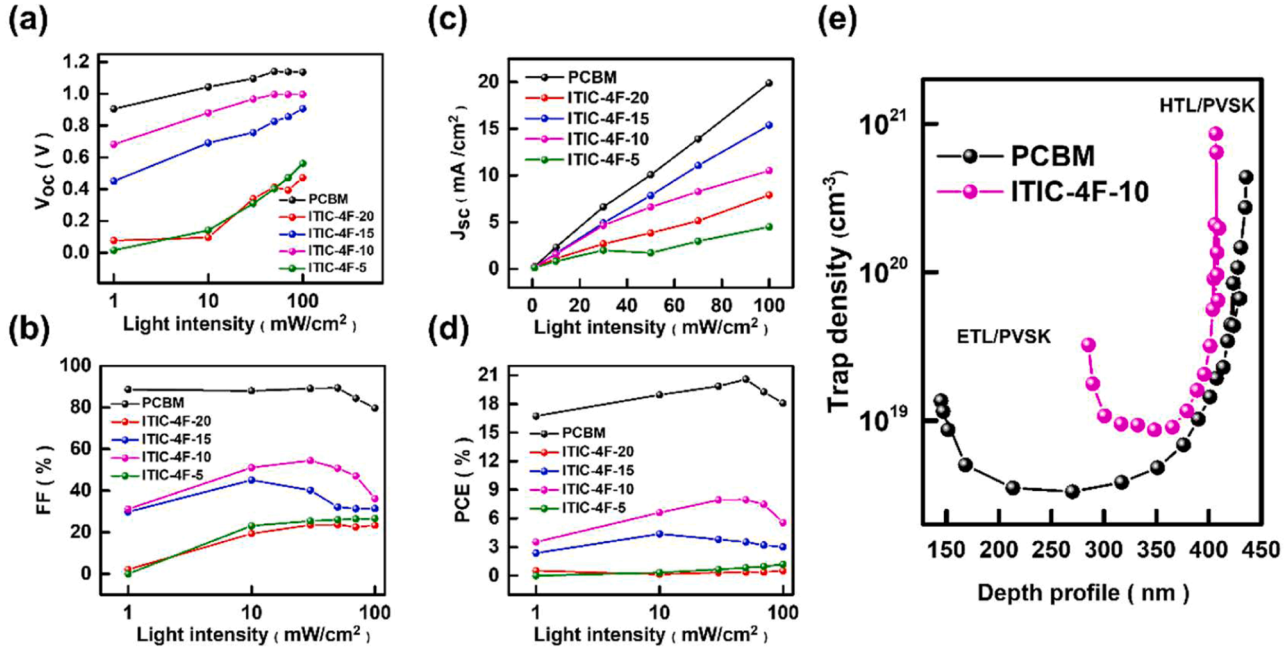

Fig. 2. Electronic diagnostic analysis of the ITIC-4F/Perovskite interface. (a–d) Light-intensity-dependent photovoltaic parameters for PSCs with PCBM and various ITIC-4F coating concentrations. (e) Spatial distribution of trap states derived from DLCP for PCBM and optimized ITIC-4F-10 devices, revealing the impact of the ETL coating on bulk and interfacial defect densities.

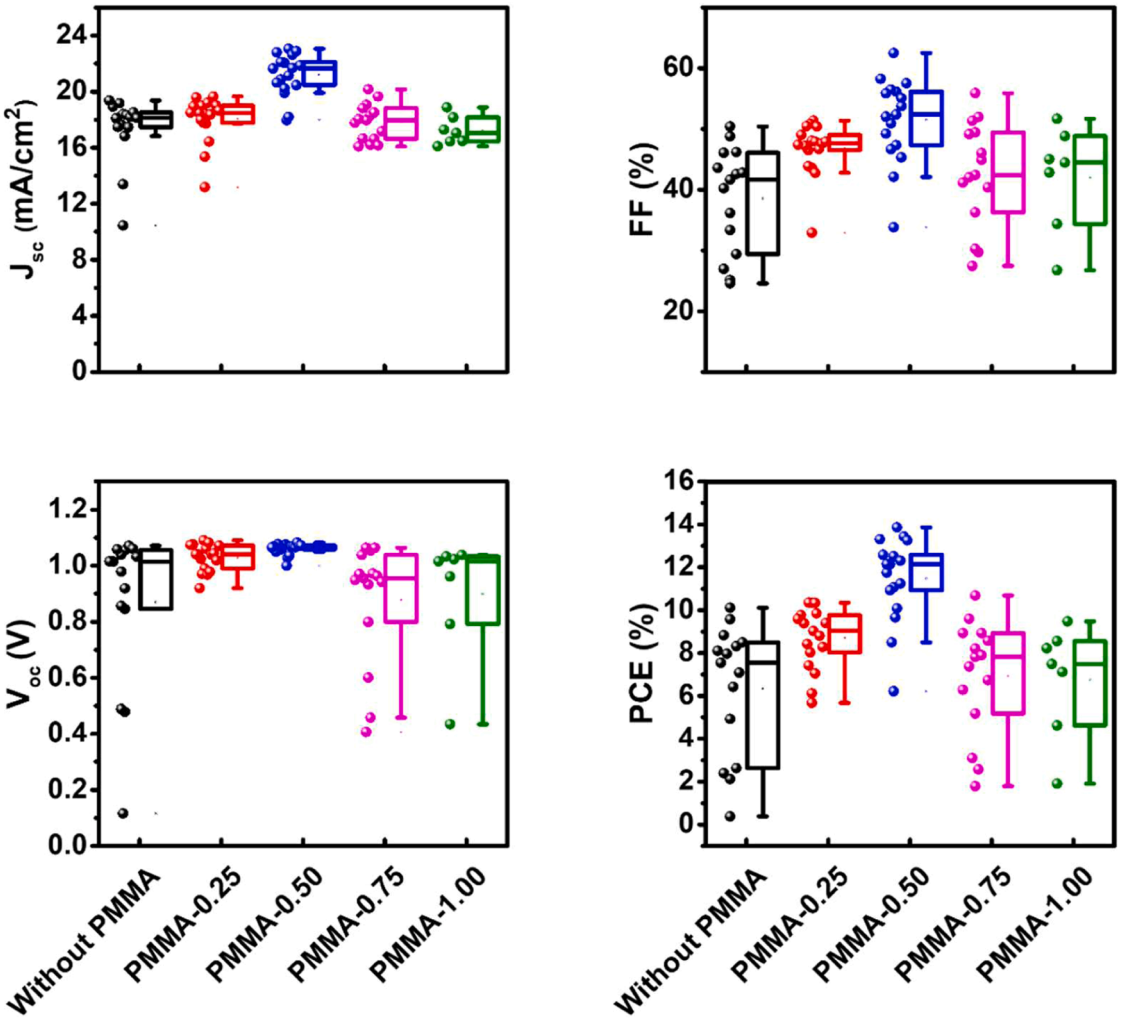

Fig. 3. Impact of the PMMA interfacial passivation layer. Statistical distribution of photovoltaic parameters for PSCs fabricated with varying PMMA interlayer concentrations (0, 0.25, 0.50, 0.75, and 1.00 mg/ml) inserted at the perovskite/ITIC-4F interface. The data highlights the trade-off between surface passivation and charge tunneling resistance.

Table 2
Photovoltaic parameters of PSCs incorporating a PMMA passivation interlayer with different coating concentrations.

Concentration of PMMA (mg/ml)	V_{oc} (V)	J_{sc} (mA/cm^2)	FF (%)	PCE (%)	R_s (ohm)	R_{sh} (ohm)
Without PMMA	0.51±0.33 (1.03)	16.45±3.68 (20.23)	30.41±6.91 (46.09)	3.24±2.97 (9.53)	183.89±61.17 (177.60)	273.93±370.31 (3277.79)
0.25	1.03±0.05 (1.04)	18.01±1.65 (19.59)	46.73±4.35 (50.83)	8.70±1.44 (10.35)	193.45±51.63 (160.69)	2574.51±929.39 (3719.40)
0.50	1.06±0.02 (1.07)	21.18±1.51 (20.86)	51.49±6.95 (62.50)	11.47±1.97 (13.87)	161.95±38.32 (119.23)	1356.93±495.16 (1750.60)
0.75	0.88±0.22 (1.06)	17.81±1.3 (19.65)	42.56±8.63 (51.32)	6.91±2.66 (10.68)	173.51±35.04 (131.46)	1088.78±580.54 (1557.10)
1.00	0.73±0.39 (1.03)	16.33±1.98 (18.87)	37.79±11.26 (48.81)	5.36±3.61 (9.47)	223.28±33.47 (143.24)	755.28±633.13 (1516.10)

mg/ml PMMA interlayer, a significant recovery in performance was observed, with the average PCE rising to 8.70%±1.44%. The performance peaked at a concentration of 0.50 mg/ml, where the devices achieved an average PCE of 11.47%±1.97%, accompanied by a V_{oc} of 1.06±0.02 V, J_{sc} of 21.18±1.51 mA cm^{-2}, and FF of 51.49±6.95%. These results indicate that the optimized PMMA interlayer effectively suppresses interfacial non-radiative recombination and improves charge extraction, primarily driven by the electronic blocking and surface passivation effects. The EQE spectra for the optimized devices are illustrated in **Figure S3**. The integrated J_{SC} values extracted from these spectra align closely with the experimental J_{SC} obtained from J-V curves, confirming the consistency and accuracy of the device performance. However, further increasing the concentration to 0.75 mg/ml and 1.00 mg/ml led to a performance roll-off, with the average PCE decreasing to 6.91%±2.66% and 5.36%±3.61%, respectively. This decline is primarily due to the reduction in average J_{sc} and FF. At higher concentrations, the excessive thickness of the insulating PMMA layer increases the tunneling barrier width, thereby introducing high series resistance

that impedes efficient charge transport. Consequently, 0.50 mg/ml was established as the optimal concentration for balancing surface passivation with charge tunneling efficiency.

As evidenced by AFM of **Figure S4**, the inclusion of this PMMA interlayer significantly smooths the ITIC-4F surface compared to the relatively rough control film. This reduced roughness ensures intimate interfacial contact and facilitates efficient charge transport between the ITIC-4F layer and the electrode. Beyond physical morphology, the polymer chains of PMMA interact with the perovskite surface via van der Waals forces, while its abundant carbonyl (C═O) functional groups act as Lewis bases to passivate undercoordinated Pb^{2+} defects. Furthermore, this ultrathin polymer matrix facilitates synergistic chemical interactions from the ETL. In **Figure S5**, Fourier-transform infrared (FTIR) spectroscopy was employed to probe the molecular interactions and functional group characteristics within the composite films. The spectra compare pristine ITIC-4F with PVSK/ITIC-4F and PVSK/PMMA/ITIC-4F architectures. Specifically, the C-S-C stretching vibration of ITIC-4F, observed at 890 cm^{-1}, undergoes a distinct shift and a significant change in intensity when interfacing with the perovskite layer. This spectral evolution indicates that the lone pair electrons from the sulfur atoms in ITIC-4F also coordinate with uncoordinated Pb^{2+} ions at the perovskite surface. The combination of PMMA's physical templating and the dual chemical passivation from both the polymer's carbonyl groups and ITIC-4F's sulfur atoms effectively suppresses the formation of interfacial trap states and minimizes non-radiative recombination, thereby contributing to the enhanced device performance [39]. Fig. 4 presents the depth-resolved trap density analysis, which corroborates the photovoltaic performance trends observed in the devices. To validate the spatial assignment of these defect states, the geometric thickness of the perovskite layer was independently measured via cross-sectional SEM (**Figure S6**), yielding an average thickness of 514 nm. Given that the maximum effective capacitive depth probed in our DLCP measurements reaches approximately 400–450 nm, the depletion region closely approaches the actual physical boundary of the active layer. Therefore, the spatial profiling accurately reflects the trap distribution, spanning from the front ETL/perovskite interface (shallower depth at forward bias) extending toward the rear HTL/perovskite interface (deeper depth). While the PCBM/BCP configuration exhibits the lowest overall trap density, the introduction of 0.5 mg/ml PMMA between the perovskite and the ITIC-4F ETL significantly reduces the density of electronic defects compared to the control device without PMMA. This reduction in trap density, particularly near the ETL/PVSK interface, confirms that the optimized PMMA interlayer effectively passivates surface trap states, thereby suppressing non-radiative recombination. However, increasing the PMMA concentration to 0.75 mg/ml and 1.00 mg/ml leads to a sharp rise in trap density across the depth profile. This apparent surge in defect density is likely indicative of charge accumulation caused by the excessive thickness of the insulating barrier, rather than the formation of new intrinsic bulk defects. The thick PMMA layer impedes efficient carrier tunneling, creating resistive barriers that mimic high recombination centers. This observation explains the subsequent decline in V_{OC} and J_{SC} at higher concentrations. Consequently, the trap density measurements identify the 0.5 mg/ml treatment as the optimal coating threshold, successfully balancing surface passivation with efficient charge transport. The cross-sectional SEM image of the optimized PSCs was provided in **Figure S6**.

To further investigate the charge-carrier dynamics and the underlying physical mechanisms responsible for the performance enhancement in the PMMA-modified devices, we performed TPC, TPV, and EIS measurements. These characterizations allow for a comprehensive understanding of how the PMMA interlayer influences charge extraction, recombination, and interfacial resistance. The charge extraction behavior at the perovskite/ITIC-4F interface was first evaluated via TPC, as shown in Fig. 5a. With the incorporation of the optimized PMMA/ITIC-4F configuration, the charge extraction time slightly increased from 0.73 μs to 0.81 μs. Although PMMA is inherently an insulating polymer, the efficient extraction time suggests that the thin layer (from 0.5 mg/ml) does not introduce a significant transport barrier. Instead, the coating maintains a tunneling-compatible thickness that allows for effective carrier sweep-out while modifying the interface. Simultaneously, the impact of the PMMA interlayer on carrier recombination was analyzed through TPV measurements, which are shown in Fig. 5b. The photovoltage decay in the PMMA-treated device was significantly prolonged compared to the control ITIC-4F device, yielding a calculated carrier lifetime (τ) of 116.94 ms. This significant increase in lifetime indicates that the PMMA layer successfully passivates surface trap states at the perovskite interface, thereby suppressing non-radiative recombination. The result directly corroborates the higher performance observed in these devices. To elucidate the impact of the PMMA interlayer on interfacial dynamics, electrochemical impedance spectroscopy (EIS) was employed. This technique enables a quantitative assessment of how polymer modification at the ETL/perovskite interface influences charge carrier transport and suppresses nonradiative recombination. These transient results are further supported by EIS analysis under different operating conditions, depicted in Fig. 5c. Under illumination, the Nyquist plots reveal a smaller semi-circle for the PMMA-modified device, indicating a reduction in charge-transfer resistance (R_{ct}). Furthermore, to evaluate the practical viability and photostability of the devices, continuous maximum power point (MPP) tracking was performed under ambient conditions (50% RH, 25 °C). The steady-state PCE

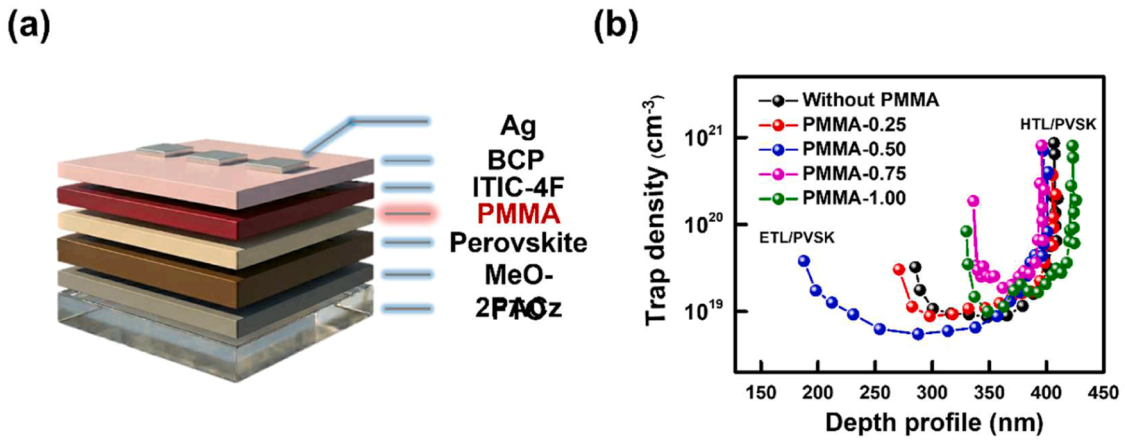

Fig. 4. Device architecture and defect distribution analysis of PSCs with varying PMMA interlayer concentrations. (a) Schematic illustration of the p-i-n device architecture. (b) Spatially resolved trap density depth profiles determined via DLCP for the control device (without PMMA) and devices incorporating PMMA interlayers at concentrations ranging from 0.25 to 1.00 mg/ml.

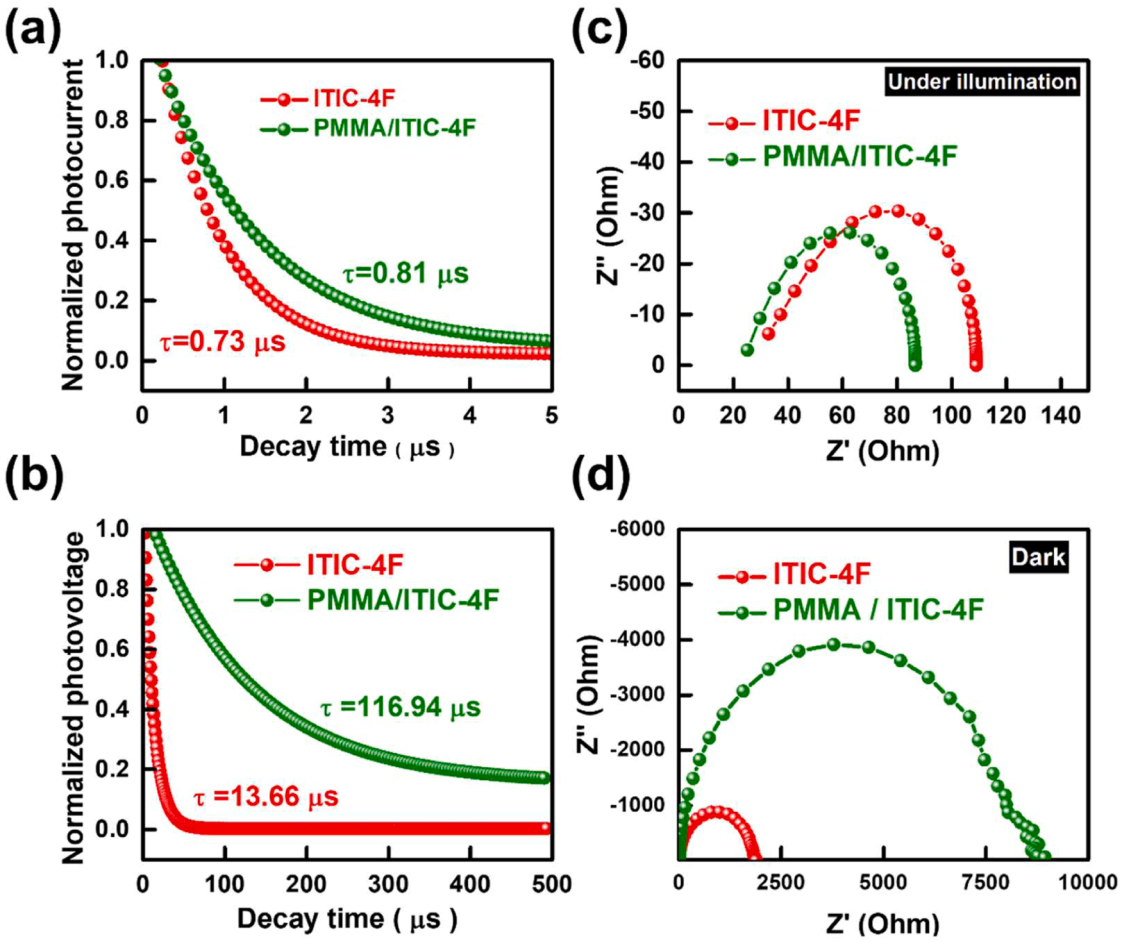

Fig. 5. Analysis of interfacial carrier dynamics and recombination kinetics. (a) TPC decay profiles and corresponding extraction times. (b) TPV decay profiles and corresponding carrier lifetimes. Nyquist plots obtained from EIS under (c) 1-sun illumination and (d) dark conditions.

was monitored periodically using an LSH-7320 LED solar simulator, with the results presented in **Figure S7**. The PSC incorporating the optimized PMMA interlayer demonstrated robust operational endurance, maintaining a highly stable steady-state PCE over the tracking period. In contrast, the control device without PMMA exhibited a lower and less stable output. This enhanced photostability is primarily attributed to the PMMA modification. Functionally, the hydrophobic nature of the PMMA matrix provides a physical barrier against moisture ingress in the ambient environment. Simultaneously, its excellent defect passivation capabilities suppress light-induced ion migration and interfacial charge accumulation, thereby mitigating light-induced degradation pathways and ensuring stable operation. This reduction signifies improved electronic contact and more efficient charge collection at the cathode interface. Conversely, EIS measurements conducted in the dark (Fig. 5d) show a significantly larger semi-circle for the PMMA/ITIC-4F device, corresponding to a recombination resistance (R_{rec}). This elevated R_{rec} confirms that the PMMA interlayer acts as an effective electronic blocking layer, minimizing leakage current and back-electron recombination. These dynamic and resistive analyses demonstrate that an optimized PMMA interlayer creates a selective interface that successfully balances rapid charge extraction with superior defect passivation.

4. Conclusion

In this work, we establish the end-fluorinated ITIC-4F as a promising candidate for fullerene-free ETL in p-i-n PSCs. While ITIC-4F offers superior hole-blocking capabilities via its deep HOMO level, our analysis identified that the pristine coating is intrinsically limited by high trap densities and severe interfacial recombination. To resolve these surface deficiencies, we implemented a strategic PMMA passivation layer to engineer the perovskite/ETL interface. This insulating polymer effectively reconstructed the surface contact, significantly reducing defect states as confirmed by DLCP profiling. Crucially, the optimized PMMA/ITIC-4F configuration enabled superior carrier dynamics, yielding an extended carrier lifetime of 116.94 ms and efficient charge extraction. Functionally, this surface repair strategy translated into an obvious performance recovery, boosting the average PCE from 3.24% to 11.47%, with a champion PCE of 13.87%. We further note that precise thickness control is essential, as excessive PMMA introduces resistive barriers that negate these benefits. Overall, our findings demonstrate that rational interfacial engineering is indispensable for unlocking the full potential of NFA-based coatings, providing a robust pathway for stable and efficient fullerene-free p-i-n PSCs.

CRediT authorship contribution statement

Shih-Han Huang: Writing – original draft, Visualization, Validation, Methodology, Investigation, Formal analysis, Data curation. **Wen-Ting Li:** Visualization, Validation, Methodology, Investigation, Formal analysis, Data curation. **Chia-Feng Li:** Investigation, Formal analysis, Data curation. **Yu-Hung Hsiao:** Investigation, Data curation. **Hou-Chin Cha:** Visualization, Data curation. **Chih-Min Chuang:** Data curation. **Yu-Ching Huang:** Writing – review & editing, Resources, Project administration, Methodology, Funding acquisition, Conceptualization.

Declaration of competing interest

The authors declare the following financial interests/personal relationships which may be considered as potential competing interests: Yu-Ching Huang reports financial support was provided by National Science and Technology Council of Taiwan. If there are other authors, they declare that they have no known competing financial interests or personal relationships that could have appeared to influence the work reported in this paper.

There are no conflicts to declare.

Acknowledgments

Financial support provided by the National Science and Technology Council of Taiwan (Grant Nos. NSTC 112-2628-E-131-001-MY4, NSTC 114-2622-E-131-007, NSTC 114-2222-E-131-002, NSTC 114-2622-E-131-015, and NSTC 114-2221-E-131-012-MY3).

Data availability

Data will be made available on request.

References

[1] Z. Xiong, Q. Zhang, K. Cai, H. Zhou, Q. Song, Z. Han, S. Kang, Y. Li, Q. Jiang, X. Zhang, J. You, Homogenized chlorine distribution for >27% power conversion efficiency in perovskite solar cells, Science 390 (6773) (2025) 638–642.
[2] M. De Bastiani, V. Larini, R. Montecucco, G. Grancini, The levelized cost of electricity from perovskite photovoltaics, Energy Environ. Sci. 16 (2) (2023) 421–429.
[3] R. Li, X. Liu, J. Chen, Opportunities and challenges of hole transport materials for high-performance inverted hybrid-perovskite solar cells, Exploration 3 (3) (2023) 20220027.
[4] H. Wei, Z. Shao, Z. Li, S. Pang, G. Cui, Enhancing efficiency in inverted perovskite solar cells: the role of dual-site binding ligands, Green Carbon 2 (3) (2024) 316–317.
[5] J. Xu, C.C. Boyd, Z.J. Yu, A.F. Palmstrom, D.J. Witter, B.W. Larson, R.M. France, J. Werner, S.P. Harvey, E.J. Wolf, W. Weigand, S. Manzoor, M.F.A.M. van Hest, J. J. Berry, J.M. Luther, Z.C. Holman, M.D. McGehee, Triple-halide wide–band gap perovskites with suppressed phase segregation for efficient tandems, Science 367 (6482) (2020) 1097–1104.
[6] Q. Jiang, K. Zhu, Rapid advances enabling high-performance inverted perovskite solar cells, Nat. Rev. Mater. 9 (6) (2024) 399–419.
[7] S.-H. Huang, K.-Y. Tian, H.-C. Huang, C.-F. Li, W.-C. Chu, K.-M. Lee, Y.-C. Huang, W.-F. Su, Controlling the morphology and interface of the perovskite layer for scalable high-efficiency solar cells fabricated using green solvents and blade coating in an ambient environment, ACS Appl. Mater. Interfaces 12 (23) (2020) 26041–26049.
[8] T. Ahmad, B. Wilk, E. Radicchi, R.F. Pineda, P. Spinelli, J. Herterich, L. A. Castriotta, S. Dasgupta, E. Mosconi, F. De Angelis, M. Kohlstädt, U. Würfel, A. Di Carlo, K. Wojciechowski, New fullerene derivative as an n-type material for highly efficient, flexible perovskite solar cells of a p-i-n configuration, Adv. Funct. Mater. 30 (45) (2020) 2004357.
[9] S.-H. Huang, C.-K. Guan, P.-H. Lee, H.-C. Huang, C.-F. Li, Y.-C. Huang, W.-F. Su, Toward all slot-die fabricated high efficiency large area perovskite solar cell using rapid near infrared heating in ambient air, Adv. Energy Mater. 10 (37) (2020) 2001567.
[10] X. Zhang, S. Wu, H. Zhang, A.K.Y. Jen, Y. Zhan, J. Chu, Advances in inverted perovskite solar cells, Nat. Photonics 18 (12) (2024) 1243–1253.
[11] C.-F. Li, S.-H. Huang, Y.-R. Chen, H.-C. Cha, S.-Y. Chung, Y.-H. Hsiao, F.-Y. Tsai, Y.-C. Huang, Sequential slot-die coating of perovskite solar cell modules under ambient conditions with precise phase-transition control, Chem. Eng. J. 517 (2025) 164194.
[12] L. Jia, M. Chen, S. Yang, Functionalization of fullerene materials toward applications in perovskite solar cells, Mater. Chem. Front. 4 (8) (2020) 2256–2282.
[13] D. Li, T. Nie, G. Zhao, R. Lv, J. Feng, J. Ding, S. Yang, S. Liu, Z. Fang, Dual optimization via doping PCBM with diamine for efficient pure-iodide wide-bandgap perovskite solar cells, Adv. Funct. Mater. 36 (4) (2025) e02847.
[14] S.-H. Huang, Y.-C. Wang, K.-C. Hsiao, P.-H. Lee, H.-C. Liao, Y.-X. Huang, Y.-C. Huang, W.-F. Su, Solid-State ligand-capped metal oxide electron-transporting layer for efficient and stable fullerene-free perovskite solar cells, Sol. RRL 6 (2) (2022) 2100671.
[15] C. Cui, Y. Li, Y. Li, Fullerene derivatives for the applications as acceptor and cathode buffer layer materials for organic and perovskite solar cells, Adv. Energy Mater. 7 (10) (2017) 1601251.
[16] W. Chen, B. Han, Q. Hu, M. Gu, Y. Zhu, W. Yang, Y. Zhou, D. Luo, F.-Z. Liu, R. Cheng, R. Zhu, S.-P. Feng, A.B. Djurišić, T.P. Russell, Z. He, Interfacial stabilization for inverted perovskite solar cells with long-term stability, Sci. Bull. 66 (10) (2021) 991–1002.
[17] J. Hou, O. Inganäs, R.H. Friend, F. Gao, Organic solar cells based on non-fullerene acceptors, Nat. Mater. 17 (2) (2018) 119–128.
[18] N. Yang, S. Zhang, Y. Cui, J. Wang, S. Cheng, J. Hou, Molecular design for low-cost organic photovoltaic materials, Nat. Rev. Mater. 10 (6) (2025) 404–424.
[19] D. Meng, J. Xue, Y. Zhao, E. Zhang, R. Zheng, Y. Yang, Configurable organic charge carriers toward stable perovskite photovoltaics, Chem. Rev. 122 (18) (2022) 14954–14986.
[20] K. Takimiya, M. Nakano, Thiophene-fused naphthalene diimides: new building blocks for electron deficient π-functional materials, Bull. Chem. Soc. Jpn. 91 (1) (2018) 121–140.
[21] R. Wang, K. Jiang, H. Yu, F. Wu, L. Zhu, H. Yan, Efficient inverted perovskite solar cells with truxene-bridged PDI trimers as electron transporting materials, Mater. Chem. Front. 3 (10) (2019) 2137–2142.
[22] Z. Qi, H. Liu, S. Zheng, Impact of terminal halogen and CN substitutions on photoelectric properties of asymmetric Y6-based NFA with terminal groups in different orientations: a DFT/TDDFT study, J. Phys. Chem. A 129 (20) (2025) 4488–4495.
[23] S. Haseena, M.V. Jyothirmai, M.K. Ravva, Rational design of fused-ring based non-fullerene acceptors for high performance organic solar cells, Sol. Energy 242 (2022) 201–211.
[24] B. Chen, F. Zheng, Q. Wang, P. Guo, Q. Liang, Y. Zhang, C. Wang, Y. Xia, H. Wu, Effect of fluorine atoms on the dielectric constants, optoelectronic properties and charge carrier kinetic characteristics of indacenodithieno[3,2-b]thiophene based non-fullerene acceptors for efficient organic solar cells, Sol. Energy 236 (2022) 206–214.
[25] X. Huang, D. Xia, Q. Xie, D. Wang, Q. Li, C. Zhao, J. Yin, F. Cao, Z. Su, Z. Zeng, W. Jiang, W. Kaminsky, K. Liu, F.R. Lin, Q. Feng, B. Wu, S.-W. Tsang, D. Lei, W. Li, A.K.Y. Jen, Supramolecular force-driven non-fullerene acceptors as an electron-transporting layer for efficient inverted perovskite solar cells, Nat. Commun. 16 (1) (2025) 1626.
[26] D. Angmo, X. Peng, J. Cheng, M. Gao, N. Rolston, K. Sears, C. Zuo, J. Subbiah, S.-S. Kim, H. Weerasinghe, R.H. Dauskardt, D. Vak, Beyond fullerenes: indacenodithiophene-based organic charge-transport layer toward upscaling of low-cost perovskite solar cells, ACS Appl. Mater. Interfaces 10 (26) (2018) 22143–22155.
[27] W. Chen, A.A. Said, Z. Wang, Y. Zhou, W. Liu, W.-B. Gao, M. Liu, Q. Zhang, Sulfur position in pyrene-based PTTIs plays a key role to determine the performance of perovskite solar cells when PTTIs were employed as electron transport layers, ACS Appl. Energy Mater. 2 (8) (2019) 5716–5723.
[28] H. Yu, Q. Zhang, C. Han, X. Zhu, X. Sun, Q. Yang, H. Yang, L. Deng, F. Zhao, K. Wang, B. Hu, Improving photovoltaic performance of inverted planar structure perovskite solar cells via introducing photogenerated dipoles in the electron transport layer, Org. Electron. 63 (2018) 137–142.
[29] Y.-J. Noh, J.-H. Jeong, S.-S. Kim, H.-K. Kim, S.-I. Na, Non-fullerene-based small molecules as efficient n-type electron transporting layers in inverted organic–inorganic halide perovskite solar cells, J. Ind. Eng. Chem. 65 (2018) 406–410.
[30] Y.-C. Huang, S.-W. Huang, C.-F. Li, S.-H. Huang, F.-Y. Tsai, W.-F. Su, A comprehensive optimization of highly efficient MA-free wide-bandgap perovskites for 4-T Perovskite/Silicon tandem solar cells, Chem. Eng. J. 503 (2025) 158272.
[31] J. Wang, Y. Xie, K. Chen, H. Wu, J.M. Hodgkiss, X. Zhan, Physical insights into non-fullerene organic photovoltaics, Nat. Rev. Phys. 6 (6) (2024) 365–381.
[32] J.M. Marin-Beloqui, D.T.W. Toolan, N.A. Panjwani, S. Limbu, J.-S. Kim, T. M. Clarke, Triplet-charge annihilation in a small molecule donor: acceptor blend as a major loss mechanism in organic photovoltaics, Adv. Energy Mater. 11 (24) (2021) 2100539.
[33] J.A. Mikroyannidis, A.N. Kabanakis, S.S. Sharma, G.D. Sharma, A simple and effective modification of PCBM for use as an electron acceptor in efficient bulk heterojunction solar cells, Adv. Funct. Mater. 21 (4) (2011) 746–755.
[34] E. Dauzon, Y. Lin, H. Faber, E. Yengel, X. Sallenave, C. Plesse, F. Goubard, A. Amassian, T.D. Anthopoulos, Stretchable and transparent conductive PEDOT:pSS-based electrodes for organic photovoltaics and strain sensors applications, Adv. Funct. Mater. 30 (28) (2020) 2001251.
[35] A. These, L.J.A. Koster, C.J. Brabec, V.M. Le Corre, Beginner's guide to visual analysis of perovskite and organic solar cell current density–Voltage characteristics, Adv. Energy Mater. 14 (21) (2024) 2400055.
[36] D. Glowienka, Y. Galagan, Light intensity analysis of photovoltaic parameters for perovskite solar cells, Adv. Mater. 34 (2) (2022) 2105920.
[37] Z. Ni, C. Bao, Y. Liu, Q. Jiang, W.-Q. Wu, S. Chen, X. Dai, B. Chen, B. Hartweg, Z. Yu, Z. Holman, J. Huang, Resolving spatial and energetic distributions of trap states in metal halide perovskite solar cells, Science 367 (6484) (2020) 1352–1358.
[38] H. Kim, K.S. Lee, M.J. Paik, D.Y. Lee, S.-U. Lee, E. Choi, J.S. Yun, S.I. Seok, Polymethyl methacrylate as an interlayer between the halide perovskite and copper phthalocyanine layers for stable and efficient perovskite solar cells, Adv. Funct. Mater. 32 (13) (2022) 2110473.
[39] S. Ryu, B. Gil, B. Kim, J. Kim, B. Park, Understanding the trap characteristics of perovskite solar cells via drive-level capacitance profiling, ACS Appl. Mater. Interfaces 15 (49) (2023) 56909–56917.